

High-Speed Nonlinear Interferometric Vibrational Imaging of Biological Tissue With Comparison to Raman Microscopy

Wladimir A. Benalcazar, Praveen D. Chowdary, Zhi Jiang, Daniel L. Marks, Eric J. Chaney, Martin Gruebele, and Stephen A. Boppart, *Senior Member, IEEE*

Abstract—Vibrational contrast imaging of the distribution of complex biological molecules requires the use of techniques that provide broadband spectra with sufficient resolution. Coherent anti-Stokes Raman scattering (CARS) microscopy is currently limited in meeting these requirements due to the presence of a nonresonant background and its inability to target multiple resonances simultaneously. We present nonlinear interferometric vibrational imaging (NIVI), a technique based on CARS that uses femtosecond pump and Stokes pulses to retrieve broadband vibrational spectra over 200 cm^{-1} (full-width at half maximum). By chirping the pump and performing spectral interferometric detection, the anti-Stokes pulses are resolved in time. This phase-sensitive detection allows suppression of not only the nonresonant background, but also of the real part of the nonlinear susceptibility $\chi^{(3)}$, improving the spectral resolution and features to make them comparable to those acquired with spontaneous Raman microscopy, as shown for a material sample and mammary tissue.

Index Terms—Biological tissue, coherent anti-Stokes Raman scattering (CARS), interferometry, nonlinear interferometric vibrational imaging (NIVI), optical imaging, spectroscopy.

I. INTRODUCTION

OVER the past decade, the development of nonlinear microscopy techniques has expanded the possibilities to visualize and characterize molecules and biological processes. The advantage of these over more conventional microscopy

techniques is that their contrast mechanisms provide high chemical selectivity without the need of external dyes or markers that may alter the chemical properties of small molecules [1].

In particular, we focus on the use of molecular vibrational contrast for imaging. This has its origins in spontaneous Raman scattering microscopy [2], a technique that can obtain high-resolution vibrational spectra over a wide range of wavenumbers, making it suitable for the identification of unique spectral features from biological species, mostly in the fingerprint region of the vibrational spectrum. Raman microscopy is used in a confocal configuration, where the sample is spatially scanned and a spectrum is collected at each position. Many studies have demonstrated this technique [3]–[8], however, the weak amplitude of the acquired signal leads to extremely long acquisition times, making it prohibitive as a clinical tool or for monitoring biological processes in real time.

As an alternative, coherent anti-Stokes Raman scattering (CARS) microscopy [9], [10] can stimulate the production of a significantly larger signal, and like spontaneous Raman, does not require the introduction of exogenous markers. In a CARS event, a pump photon of frequency ω_p and a Stokes photon of frequency ω_s are tuned to have a difference in frequency $\omega_p - \omega_s = \Omega$ that matches the vibrational frequency Ω of a molecular bond of interest. The interaction of these two photons with the sample populates an excited vibrational state, and when a probe photon of frequency $\omega_{p'}$ interacts with this state, an anti-Stokes photon of frequency $\omega = \omega_p + \omega_{p'} - \omega_s$ is emitted as the signal of interest.

CARS has been used in a variety of biological applications, most commonly related to mapping lipids and protein domains in cells [11]. Its fast acquisition has allowed live cell imaging [12], [13] and intracellular organelle tracking [14]. Other applications include imaging of the myelin sheath and brain structures [15], [16], and the evaluation of the impact of obesity on mammary gland and tumor stroma [17], to name a few.

Nevertheless, the CARS microscopy technique faces two important challenges that must be overcome to improve its chemical selectivity. The first is to suppress an overlapping nonresonant background caused by electronic responses in molecules [18]. This background is independent of the Raman shift and coherently interferes with the resonant signal, broadening, and shifting the spectral peaks [19].

Several methods to suppress this background have been developed. Techniques such as polarization-sensitive [18] and time-resolved [20] CARS have proven successful in decreasing the

Manuscript received August 20, 2009; revised October 21, 2009; accepted October 21, 2009. Date of publication December 4, 2009; date of current version August 6, 2010. This work was supported in part by the National Institutes of Health's National Cancer Institute under Grants R21/R33 CA115536, and in part by the National Institute of Biomedical Imaging and Bioengineering under Grant R01 EB005221, awarded to Stephen Boppart as Principal Investigator.

W. A. Benalcazar is with the Department of Electrical and Computer Engineering, Biophotonics Imaging Laboratory, Beckman Institute for Advanced Science and Technology, University of Illinois at Urbana-Champaign, Urbana, IL 61801 USA (e-mail: wbenalc2@illinois.edu).

P. D. Chowdary is with the Department of Chemistry, University of Illinois at Urbana-Champaign, Urbana, IL 61801 USA (e-mail: praveen@scs.uiuc.edu).

Z. Jiang, D. L. Marks, and E. J. Chaney are with the Biophotonics Imaging Laboratory, Beckman Institute for Advanced Science and Technology, University of Illinois at Urbana-Champaign, Urbana, IL 61801 USA (e-mail: zjiang@illinois.edu; dmarks@illinois.edu; echaney@illinois.edu).

M. Gruebele is with the Departments of Chemistry, Beckman Institute for Advanced Science and Technology, University of Illinois at Urbana-Champaign, Urbana, IL 61801 USA (e-mail: gruebele@scs.uiuc.edu).

S. A. Boppart is with the Departments of Electrical and Computer Engineering, Bioengineering, and Medicine, Biophotonics Imaging Laboratory, Beckman Institute for Advanced Science and Technology, University of Illinois at Urbana-Champaign, Urbana, IL 61801 USA (e-mail: boppart@illinois.edu).

Color versions of one or more of the figures in this paper are available online at <http://ieeexplore.ieee.org>.

Digital Object Identifier 10.1109/JSTQE.2009.2035537

amount of nonresonant background, but at the expense of reducing the SNR.

The second challenge is the need for probing multiple resonances simultaneously. In order to do this, and contrary to spontaneous Raman scattering, CARS requires the use of broadband excitation pulses (i.e., femtosecond pulses). Initially, picosecond pulses were used because they have the same spectral width as single vibrational lines, and thus, minimize the generation of nonresonant processes. However, this comes at the expense of losing spectral content, a necessary requirement to identify complex biological compounds that need broad vibrational spectra to be characterized. To overcome this, multiplex CARS [21], [22] probes multiple modes simultaneously by the use of picosecond pump and femtosecond Stokes pulses, but the nonresonant background distorts the vibrational spectra.

A recent important method to reject the background was to take advantage of the coherent properties of CARS signals and perform interferometric detection [23]–[30]. In this scheme, the anti-Stokes pulses from the sample are mixed with pulses in the same frequency range from a local oscillator, resulting in phase-sensitive measurements. When broadband pulses are used in multiplex interferometric CARS schemes using spectral interferometry [31]–[33], the retrieved spectra resemble those acquired using spontaneous Raman spectroscopy. Alternatively, numerical algorithms using the maximum entropy method for discrimination of the resonant signal have been used [34], simplifying the optical set up, but at the expense of lengthening the processing time.

In previous work, we described NIVI as a method for restoring resonant anti-Stokes spectra acquired from broadband chirped pulses and interferometric detection, and demonstrated the principle for isopropanol [32]. We now demonstrate vibrational imaging obtained with this technique, and show its ability to restore pure resonant vibrational spectra from highly scattering biological tissue by comparing it with spontaneous Raman spectroscopy. The use of chirped pulses represents a simplified alternative to more elaborate methods that provide control over the incident pulses, such as those using pulse-shaping systems [28], [35]. The use of chirped pulses in the retrieval of the CARS signal has been demonstrated in the past [36], [37], but without interferometric detection.

In the next section, a theoretical description of the technique is presented. An overview of the experimental system setup and its main features follows in Section III. In Section IV, vibrational imaging and comparisons to Raman spectra from both a material sample and mammary tissue are shown and discussed, and conclusions are given in Section V.

II. PRINCIPLES OF OPERATION

A CARS process for narrow band pulses follows the description provided in Section I. For the case of broadband pulses, consider a sample characterized by the third-order nonlinear susceptibility $\chi^{(3)}(\Omega)$ that is illuminated by a broadband field E , which provides all the incident photons (i.e., pump, Stokes, and probe photons). Here, Ω are the vibrational frequencies of

the molecule. A CARS process can be separated into two steps as follows:

Step 1:

$$N(\Omega) = \chi^{(3)}(\Omega) \int_0^\infty E(\omega_s + \Omega)E(\omega_s) d\omega_s \quad (1)$$

Step 2:

$$P^{(3)}(\omega) = \varepsilon_0 \int_0^\omega E(\omega - \Omega)N(\Omega) d\Omega \quad (2)$$

where ω_s and ω are the Stokes and anti-Stokes frequencies. The pump frequencies correspond to $\omega_p \equiv \omega_s + \Omega$. In step 1, corresponding to (1), the molecules respond to the instantaneous beating frequencies of the pump and Stokes fields (optical oscillations corresponding to the carrier frequencies of the fields are too fast to drive the motion of the heavy nuclei of the molecules). As a result, a population $N(\Omega)$ is created that resembles $\chi^{(3)}(\Omega)$, but is modulated by the spectral cross correlation of the pump ($E(\omega_s + \Omega)$) and Stokes ($E(\omega_s)$) fields. Here, it is assumed that the sample does not interact directly with any of the frequencies inside the bandwidth of the incident field, a safe assumption to make with the use of near-infrared light, since its energy is above vibrational resonances, but below electronic transitions.

In Step 2, corresponding to (2), the probe field interacts with the populated excited states $N(\Omega)$ to give rise to the third-order nonlinear polarization $P^{(3)}(\omega)$, which then radiates the anti-Stokes field. Despite the difficulty of losing a pairwise correspondence between anti-Stokes photons and vibrational frequencies when broadband probes are used (i.e., there could be more than one vibrational frequency that maps to the same anti-Stokes frequency in (2)), there is a linear relationship of $P^{(3)}(\omega)$ with $N(\Omega)$, and therefore, with $\chi^{(3)}(\Omega)$. A deconvolution that restores the pairwise correspondence suffices to restore the vibrational signatures in $\chi^{(3)}(\Omega)$.

The most direct way to recover $\chi^{(3)}(\Omega)$ is by use of multiplex CARS [21], in which ~ 10 ps pump/probe pulses and ~ 100 fs Stokes pulses are used. In this case, no deconvolution in (2) is needed. The spectral resolution in the vibrational frequency is limited by the spectral width of the pump pulses, and the vibrational bandwidth is determined by the bandwidth of the Stokes field.

In our experiment, we decouple these two steps ((1) and (2)) in time (see Fig. 1). Just as in conventional multiplex CARS, we use one beam to serve as the pump and probe fields and another beam of lower frequency for the Stokes field. The difference is that in this case, both pump/probe and Stokes are broadband (~ 100 fs pulses when transform limited). The pump is heavily chirped to extend its temporal waveform to ~ 6 ps, and the beginning of this waveform in time is made coincident with the beginning of the transform-limited Stokes pulse. The process in Step 1 occurs only during the time in which the pump and Stokes pulses overlap. Since only a small initial portion of the pump pulse bandwidth interacts with the Stokes pulse, population of the vibrational states is excited in a range limited by the Stokes bandwidth. In addition to this population, nonresonant background will be generated. The process in Step 2 occurs during the entire duration of the pump/probe pulse, or until the

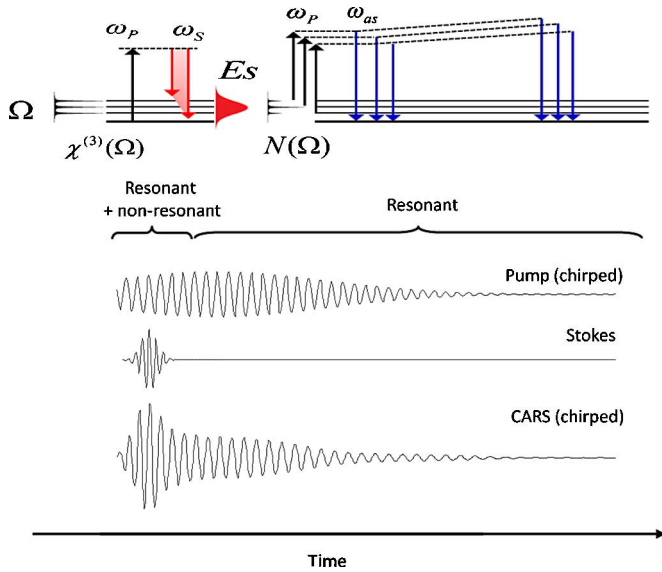


Fig. 1. Schematic of the excitation of a CARS event with broadband chirped pump pulses and broadband transform-limited Stokes pulses in NIVI. Nonresonant responses are minimized by probing the sample in the absence of the Stokes pulses.

molecular excitation has completely decayed (due to dephasing and energy relaxation [20]). Since the Stokes pulse is absent for most of the probing time, the energy of the probe pulse is efficiently used in the production of only resonant signal. Note that $N(\Omega) = 0 \forall \Omega < 0$ and because photons well above resonances are used in CARS, $N(\Omega) = 0 \forall \Omega > \omega$. Therefore, it is acceptable to change the limits of integration in (2) to cover the whole range of the spectrum. Applying the inverse Fourier transform to step 2, the third-order nonlinear polarization in time is

$$P^{(3)}(t) = \varepsilon_0 E_p(t) N(t) \quad (3)$$

where $E_p(t)$ is the pump/probe field in the time domain and $N(t)$ is defined as the Fourier transform of the population $N(\Omega)$ (For an ultrabroadband Stokes, $N(t)$ approaches $\chi^{(3)}(t)$, the vibrational impulse response of the molecule). By knowing the evolution in time of both the pump and the collected signal, $N(t)$ can be obtained, which resembles the inverse Fourier transform of $\chi^{(3)}(\Omega)$. We measure the anti-Stokes evolution in time by the use of spectral interferometry, and estimation of the temporal shape of the pump pulse is facilitated by the introduction of the positive chirp [32].

By multiplying the anti-Stokes signal $P^{(3)}(t)$ by the complex conjugate chirp of the pump, we obtain $N(t)$. Since the pump is heavily chirped, it is reasonable to neglect its slowly varying envelope. A simple Fourier transform then suffices to restore a weighted version of $\chi^{(3)}(\Omega)$ over the frequency range determined by the Stokes spectrum. The effect of neglecting the slowly varying term in the compensation of the chirp is to lower the spectral resolution of the system.

Resolving the anti-Stokes signal in time has the advantage of being sensitive to the relative phase of the different spectral components of the anti-Stokes pulses. We use this to reject 1) the nonresonant background generated in Step 1, and 2) the real

part of the susceptibility, to approach the spectral resolution of spontaneous Raman spectroscopy.

A. Heterodyne Detection and Suppression of Background

Unlike spontaneous processes like Raman scattering or fluorescence, there is a definite relation between the phases of the incident and scattered photons in CARS, which is given by the frequency response of the resonances $\chi^{(3)}(\Omega)$ that have the form

$$\chi^{(3)}(\Omega) = \sum_n \frac{A_n}{\Omega_n - i\Gamma_n - \Omega} + \chi_{nr}^{(3)} \quad (4)$$

where A_n , Ω_n , and Γ_n are, respectively, the amplitude, the frequency of resonance, and the half-width at half-maximum (HWHM) of the n^{th} vibrational mode. The term $\chi_{nr}^{(3)}$ is the frequency-independent nonresonant contribution. For a molecule with a single resonance, excitation frequencies $\Omega = \omega_p - \omega_s$, far below the frequency of resonance Ω_1 , result in anti-Stokes oscillations in phase with the incident fields. In resonance, the scattered photons are retarded in phase by $\pi/2$ and for frequencies far above resonance, they are retarded by π . On the other hand, the spectral gain of the nonresonant background is flat and its phase is close to 0 [19].

These phase relations allow discrimination of the resonances from the background. To explain how this is done, consider the anti-Stokes signal with both resonant and nonresonant components as follows:

$$P^{(3)}(\omega) = A(\omega) e^{i\phi(\omega)} \left[\text{Re}\chi_r^{(3)}(\omega) + i\text{Im}\chi_r^{(3)}(\omega) + \chi_{nr}^{(3)} \right] \quad (5)$$

where $A(\omega)$ is a slow varying real spectral envelope that collectively accounts for the modulations due to the incident fields, the attenuation in the detectors, the filter that separates the anti-Stokes signal from the incident fields, and the quantum efficiency of the camera. The term $\phi(\omega)$ is the phase responsible for the chirp, and $\chi^{(3)}(\omega)$ is the vibrational gain of the optical anti-Stokes frequencies. If this anti-Stokes signal is mixed with a reference signal $R(\omega)e^{-i\omega\tau}$, with $R(\omega)$ being real, then at the spectrometer, each frequency interferes separately, so that the spectral power of the cross-interference term obtained along the camera is

$$A(\omega)R(\omega) \{ \alpha \cos(\phi(\omega) - \omega\tau) - \beta \sin(\phi(\omega) - \omega\tau) \} \quad (6)$$

with $\alpha = \text{Re}(\chi_r^{(3)}(\omega)) + \chi_{nr}^{(3)}$ and $\beta = \text{Im}(\chi_r^{(3)}(\omega))$. The signal of interest β and the background α are in quadrature. The sequence of events to retrieve the vibrational signatures is as follows. The spectral interferogram acquired at the line scan camera is transformed to the temporal domain and the slowly varying self-interference terms are suppressed with a high-pass filter. Causality is imposed by setting the components corresponding to negative times of this time resolved signal to zero. This restores the complex analytic signal of the anti-Stokes pulse. At this point, the chirp in the anti-Stokes signal is removed by multiplying the acquired temporal waveform by an opposite chirp to that of the pump. In doing so, the pairwise correspondence between anti-Stokes and vibrational frequencies is restored. By

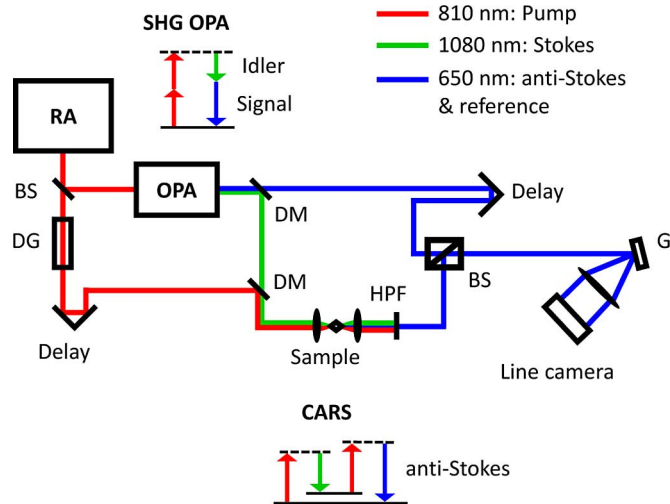


Fig. 2. Schematic of the experimental setup. BS, beam splitter; DG, dispersive glass; DM, dichroic mirror; G, diffraction grating; HPF, high-pass filter; OPA, optical parametric amplifier; RA, regenerative amplifier.

taking the Fourier transform of this resulting signal, the complex spectrum $\chi^{(3)}(\omega)$ is obtained, weighted by the spectrum $A(\omega)R(\omega)$. In practice, there are subtle phase instabilities due to mechanical noise in the setup or variations in the optical path length in the sample (i.e., changes in the refractive index and/or thickness of the sample) that do not allow for the recovery of the absolute phase of $\chi^{(3)}(\Omega)$. Nevertheless, this is easily overcome by choosing a point out of the region of the resonances and forcing it to be in zero phase. Once the absolute phase is corrected, the resulting signal is the complex third-order nonlinear susceptibility $\chi^{(3)}(\omega)$, with its imaginary part corresponding to the pure resonant vibrational response of the molecule. Finally, calibration of the spectrometer and the delay between the pump and Stokes signals allows direct mapping of $\chi^{(3)}(\omega)$ into $\chi^{(3)}(\Omega)$ and the vibrational characterization of the molecule is obtained.

III. EXPERIMENTAL SETUP

Performing heterodyne detection for CARS requires nonlinear interferometry, in which a separate coherent nonlinear process has to generate the reference pulses in the range of frequencies of the anti-Stokes signal (alternatively, supercontinuum generation can be used in the production of ultrashort pulses, from which the high-frequency portion can be used, as shown in [29]). In the present setup, the output of a second-harmonic generation, optical parametric amplifier (OPA) is used as a reference in a Mach-Zehnder interferometer.

An illustration of the system is shown in Fig. 2. A regenerative amplifier (RegA 9000, Coherent, Inc. Santa Clara, CA) emits pulses at 250 kHz repetition rate with 808 nm center wavelength and 25 nm bandwidth (full-width at half maximum). These pulses are used both as the pump and as a seed for the second-harmonic-generation OPA (OPA 9450, Coherent), which generates an idler for use as a Stokes pulse and a signal to be used as a reference for the anti-Stokes radiation. Because

the signal pulse is converted by nonresonant nonlinearities, it is reasonable to assume that the pulses are transform limited (this is a strong condition to effectively identify the phase change of the anti-Stokes photons and discriminate the resonant and nonresonant components). The duration of the pulses out of the OPA is ~ 100 fs. The pump pulses are dispersed by an 85-cm BK7 glass bar to temporally expand them to ~ 6 ps by inducing a heavy chirp. The pump and the Stokes beams are combined and focused onto the sample by an objective lens (OLYMPUS, 60 \times , 0.9 numeric aperture (NA)). The sample is placed on a translation stage for raster scanning. A delay is included in the pump path to temporally overlap the beginning of the pump and Stokes pulses at the sample. The resulting anti-Stokes signal is collected in the forward direction and is separated from the incident beams with a high-pass filter. The anti-Stokes pulses meet the reference pulses from the OPA in a beam splitter and the combined signal is spatially filtered by a pinhole and diffracted by a grating. Finally, the diffracted signal is focused on a line scan camera. A second delay is included in the reference path to adjust the delay τ in (6) and assure the interference fringes on the line camera of the spectral interferometer are within the resolution limits of the camera.

Acetone was used to find the second-order dispersion constant that chirps the pump. Its single resonance at 2925 cm^{-1} measures the degree to which the chirp in the anti-Stokes signal is corrected. By minimizing the width of the spectral peak, this constant was found to be $3.9 \times 10^{-4} \text{ fs}^2$. To calibrate the wavelength scales on the charge-coupled device (CCD) camera, the signal from silicone, which has two strong resonant peaks, was sent to both the CCD camera and a commercial spectrometer. Finally, the initial pump wavelength that interacts with the Stokes in the population of the states was adjusted by fitting the processed final term $\text{Im}(\chi^{(3)}(\Omega))$ with the one acquired with spontaneous Raman microscopy.

A nonresonant sample was used to determine the Stokes profile. This demonstrated a bandwidth of 200 cm^{-1} for this setup. The vibrational resolution was estimated to be 10 cm^{-1} and is limited by the portion of the pump bandwidth that interacts with the Stokes field. The current lateral resolution is $\sim 2 \mu\text{m}$. Spectrograms are acquired at a rate of 1 kHz. Ten acquisitions are averaged in the construction of each spatial spectrogram, resulting in an integration time of 10 ms.

IV. RESULTS AND DISCUSSION

We now present spectra and images from a material sample and mammary tissue obtained with nonlinear interferometric vibrational imaging (NIVI). These are compared with those acquired with a commercial Raman microscope (Senterra, Bruker, Billerica, MA). Because signatures obtained with spontaneous Raman microscopy are purely resonant, these signatures constitute a good standard against which the fidelity of the reproduction of spectral features in NIVI can be tested.

A. Silicone-Silicate Sample

A material sample is used to demonstrate and characterize the principles of NIVI. It consists of sodium silicate embedded

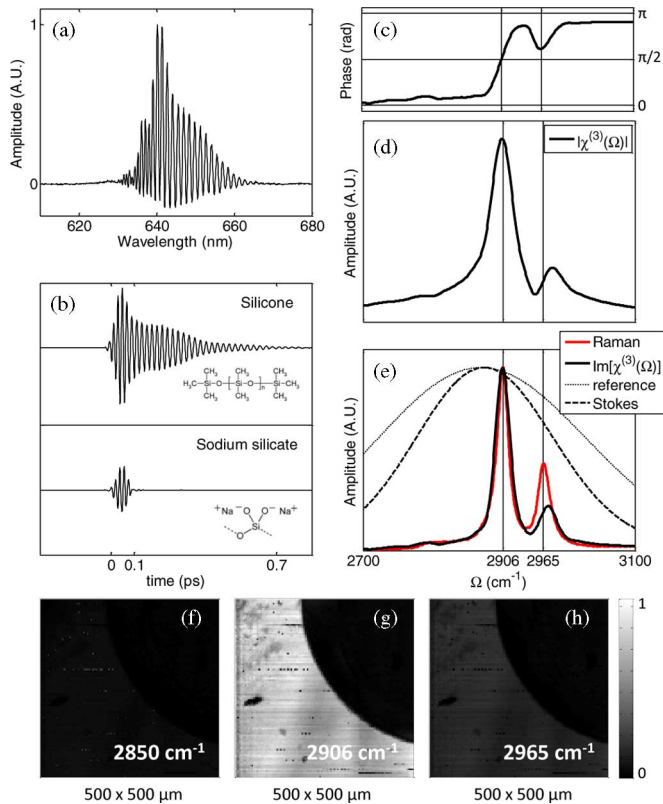


Fig. 3. Reconstruction of the spectra of silicone in the material sample. (a) Interference pattern at spectrometer. (b) Time evolution of the anti-Stokes signal (for both silicone and sodium silicate). (c) Phase and (d) magnitude of the complex vibrational spectrum $\chi^{(3)}$. (e) Obtained $\text{Im}(\chi^{(3)})$ and spontaneous Raman spectra. Dotted lines indicate the Stokes and reference spectral profiles. Images of sample (f) out of resonance at 2850 cm^{-1} and at resonances (g) 2906 cm^{-1} and (h) 2965 cm^{-1} .

in silicone. Since sodium silicate is polar and silicone is not, no mixing of the two substances occurs. The Stokes center wavelength was tuned to detect resonances in the region $2800\text{--}3000\text{ cm}^{-1}$. Silicone presents peaks at 2906 and 2965 cm^{-1} associated with its CH-stretching modes, while sodium silicate does not have any resonances in this region.

Vibrational spectra for the sample are shown in Fig. 3. Intermediate steps in the retrieval of the spectrum are shown, including the interference fringes at the line scan camera (see Fig. 3(a)), and the reconstruction of the temporal evolution of the anti-Stokes signal (see Fig. 3(b)). The duration of the entire pulse is 0.7 ps for silicone and 0.1 ps for silicate.

Because the pump pulses are almost one order of magnitude longer than the Stokes pulses, the two steps described earlier for CARS can be easily identified. Upon the arrival of the combined pump and Stokes pulses, their interaction with the sample generates resonant and nonresonant components for silicone, and only nonresonant responses for sodium silicate (0 to 0.1 ps in Fig. 3(b)). While nonresonant components respond instantaneously, the resonances of the vibrational excitations remain until they reach their decaying time ($\sim 1\text{ ps}$), so that when only the pump is acting over the sample after the Stokes is depleted (0.1 to 0.7 ps in Fig. 3(b)), only resonant signal is generated for silicone. This is corroborated by the absence of signal coming

from silicate. Fig. 3(c) and (d) shows the phase and magnitude of the retrieved $\chi^{(3)}(\Omega)$. In the presence of nonresonant background, the peaks in the magnitude are shifted, but the background is small enough to make this evident only in the peak at 2965 cm^{-1} . The phase information (see Fig. 3(c)) indicates the predicted behavior for a double Lorentzian response [as described by (4)], with frequencies below resonances in phase with the incident Stokes field, retarded by about $\pi/2$ at resonances, and out of phase by π above them. This phase information obtained by heterodyne detection allows full suppression of the nonresonant background and the real component of the resonant signal, so that the imaginary part of $\chi^{(3)}(\Omega)$ is obtained. This is shown in Fig. 3(e) in comparison with a spontaneous Raman spectrum. Both were acquired in the same region of the sample with an integration time of 50 s for Raman and 10 ms for NIVI. A reduction in the relative amplitude of the second resonance at 2965 cm^{-1} is observed as a consequence of the weight of the Stokes and reference spectra, as described in Section II. Note, however, that the spectral widths of the resonances follow those for spontaneous Raman.

By raster scanning the sample, 2-D spatial maps of 100×100 pixels of spectra are acquired in 100 s , resulting in a hyperspectral cube of information with two spatial dimensions and one spectral dimension. In Fig. 3(f)–(h), images at particular wavenumbers are shown for the corner of a silicate sphere in a silicone background. In these images, contrast increases as wavenumbers are selected from no resonance at 2850 cm^{-1} in Fig. 3(f) to resonance in silicone at 2906 cm^{-1} in Fig. 3(g). Less contrast is found at 2965 cm^{-1} for the small silicone resonance in Fig. 3(h).

B. Mammary Tissue

According to the American Cancer Society, it is estimated that 62 280 new cases of *in situ* breast cancer will occur in women in the U.S. in 2009, with 40 610 of them resulting in deaths. There exists a certain need for understanding the molecular mechanisms of tumor formation and progression, as well as for the development of new molecular detection methods with greater sensitivity. These needs motivate the demonstration and application of NIVI in mammary tissue.

We use normal mammary tissue from a nonlactating female rat. The animal care and handling was performed under a protocol approved by the Institutional Animal Care and Use Committee (IACUC) at the University of Illinois at Urbana-Champaign. The sample was resected from a euthanized animal, flash-frozen, sectioned, and mounted on a microscope slide for NIVI imaging. Serial sections of the tissue were stained with hematoxylin and eosin as per standard histological procedures and used for comparison.

Fig. 4 shows the retrieval of NIVI spectra for the cross section of mammary tissue. The real component of the time evolution of the vibrational response is shown in Fig. 4(a). The duration of the entire pulse is about $\sim 1\text{ ps}$. A beating frequency is observed as the result of the interference of the peaks at 2855 and 2930 cm^{-1} . Such temporal characterization has been studied previously, but not within a single pulse. Instead, the probe pulse

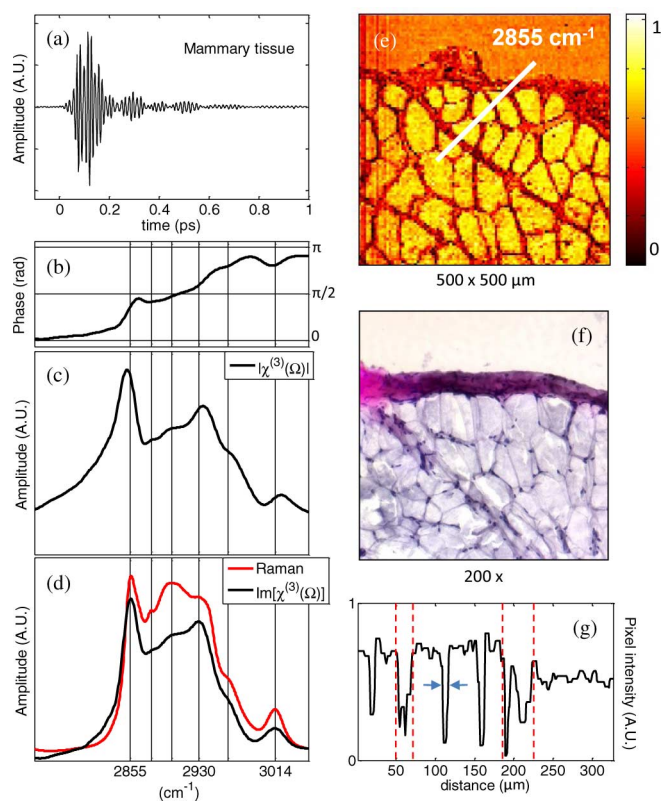


Fig. 4. Vibrational image of mammary tissue. (a) Temporal evolution of the anti-Stokes beam. (b) Phase and (c) magnitude of the retrieved susceptibility. (d) Imaginary component of the susceptibility in comparison with spontaneous Raman spectrum. (e) NIVI hyperspectral cube image at 2855 cm^{-1} showing adipocytes, parenchyma, and connective tissue. (f) Stained histological (hematoxylin & eosin) image of sample in similar region. (g) Profile of NIVI image intensity along white line in (e). Dotted red lines delineate connective tissue, extracellular matrix, and parenchyma from adipocytes. Arrows indicate extracellular space between cells.

is short in time (~ 100 fs), and a delay with respect to femtosecond pump and Stokes pulses is changed as the anti-Stokes signal power is measured [20]. The phase and magnitude obtained from this pulse are shown in Fig. 4(b) and (c). The phase changes from 0 before resonances to π after resonances. Removal of the real components results in the spectrum shown in Fig. 4(d) with a spontaneous Raman spectrum. Notice that by comparing this imaginary component with the magnitude of the obtained $\chi^{(3)}(\Omega)$, there is a satisfactory restoration of the shift in the spectral peaks induced by the real components. Since the Raman and NIVI spectra were not taken at exactly the same positions, the main difference resides in the relative intensity of these peaks (i.e., different concentration of chemical species and conformations), with the added effect of the Stokes and responses of the system being non uniform, as noted previously. Nevertheless, the six spectral features observed in this region can be discriminated [marked with vertical lines in Fig. 4(b)–(d)], and their chemical bond correspondence is shown in Table I, as assigned in the literature for the case of breast tissue [38].

In Fig. 4(e), a vibrational image (100×100 pixels) of the cross-sectional mammary layer at 2855 cm^{-1} is shown over an area of $500\text{ }\mu\text{m} \times 500\text{ }\mu\text{m}$. The acquisition time was

TABLE I
TARGETED SPECTRAL PEAKS IN MAMMARY TISSUE CAPTURED BY RAMAN MICROSCOPY AND NIVI

Raman Frequency (cm^{-1})	Group Resonance [38]
2855	$-\text{CH}_2$ symmetric
2877	$-\text{CH}_2$ asymmetric
2900	$-\text{CH}_3$ symmetric
2935	$-\text{CH}_3$ symmetric
2965	$-\text{CH}_3$ asymmetric
3014	$=\text{CH}$

100 s (10 ms/pixel) and the sample was illuminated with 10 mW of pump power and 2 mW of Stokes power. The high signal shown in bright yellow corresponds to white adipocytes, which play a crucial role in the morphogenesis of the mammary parenchyma [39], [40]. These cells contain a large lipid inclusion, composed primarily of triglycerids and cholesteryl ester (both rich in CH_2), surrounded by a layer of cytoplasm and very few mitochondria [41]. Nuclei can be distinguished as small black dots (low fat content) at the periphery of the cells. These image-based findings correlate strongly with the corresponding histological image (hematoxylin & eosin) from a similar adjacent region in the same tissue and animal, as shown in Fig. 4(f).

The thick dark-appearing boundary layer along the top portion of the tissue in Fig. 4(e) corresponds to the parenchyma, which is also clearly distinguished as the pink and dark purple layer in the histology shown in Fig. 4(f). Above this layer, anti-Stokes signal is collected from the fixative compound necessary for sectioning, which can be spectrally identified and separated. The vertical lines observed along the left side of the NIVI image are artifacts caused by the acceleration mechanism on the translational stage.

In Fig. 4(g), an intensity profile from along the white line in Fig. 4(e) reveals an estimated diameter for the cells of $\sim 50\text{ }\mu\text{m}$. Inspection of other zones within the image indicates diameters varying from 30 to $100\text{ }\mu\text{m}$. The narrow and wide regions between the dotted red lines correspond to connective tissue fibers ($\sim 25\text{ }\mu\text{m}$ thick) and the extracellular matrix ($\sim 45\text{ }\mu\text{m}$ thick), which have less lipid content and therefore less signal at the CH_2 resonance. The optical spatial resolution of $\sim 2\text{ }\mu\text{m}$ is not apparent because the step size of the image is $5\text{ }\mu\text{m}$, but this is sufficient to resolve the lipid intermembrane spaces, as indicated by arrows in Fig. 4(g).

In addition to the spectral features obtained for lipids, mostly present in the adipose cells that comprise much of the mammary tissue, a different signature has been identified for connective tissue, which is rich in collagen [42]. NIVI spectra from lipid and collagen domains in mammary tissue and Raman spectra for methyl oleate (a good model for the lipid features in breast tissue [38]), and collagen type I (Sigma Aldrich) are shown in Fig. 5(a)–(d), respectively. Similarities in the NIVI and Raman spectra for each domain are evident. The quality and fidelity of the spectra are due to the suppression of the background and the acquisition of an entire spectrum in a single measurement (for comparison with a conventional CARS spectrum of collagen in biological medium, see [43]).

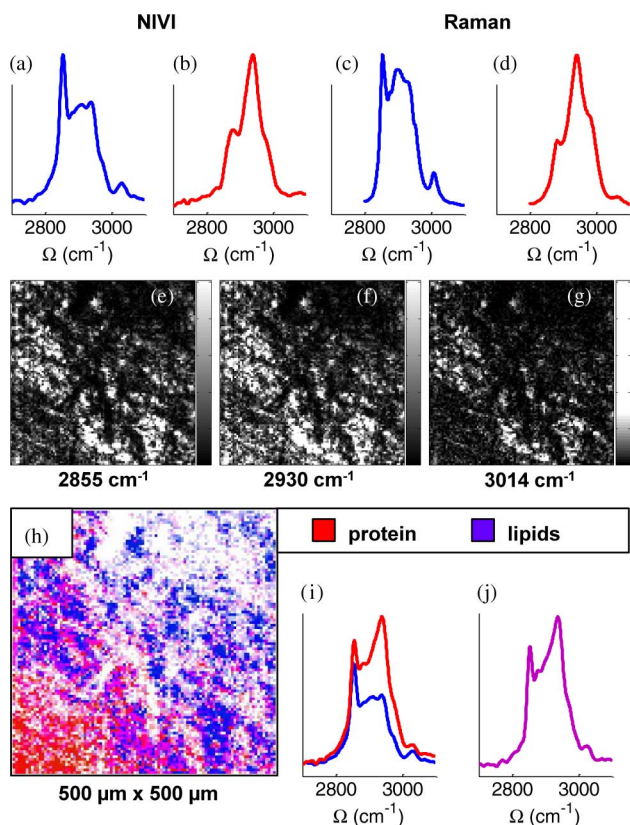


Fig. 5. Molecular differentiation in mammary tissue. (a) Lipid and (b) protein spectra from mammary tissue obtained with NIVI. (c) Methyl oleate and (d) collagen type I spectra obtained with spontaneous Raman microscopy. Images at resonances (e) 2855, (f) 2930, and (g) 3014 cm^{-1} . (h) NIVI image showing spatial differentiation of lipid and protein domains. (i) Reconstruction of the spectrum shown in (j) as a linear combination of the basis functions in (a) and (b) for a pixel with similar concentrations of proteins and lipids.

The main spectral difference between these two domains is in the ratio of the vibrational peaks at 2855 and 2930 cm^{-1} . Distinguishing and determining the proportions of protein and lipid content in breast tissue may be useful in the detection of disease. For example, it has been shown using vibrational spectroscopy that there is an increase in protein content and a decrease in lipid content in breast tumors, compared to normal tissue [38].

Broadband microspectroscopy enhances the molecular selectivity. In particular, the two domains in mammary tissue can be identified. Within the scope of this paper, we do not intend to quantitatively characterize the concentrations of these two domains. However, this is the subject of ongoing research.

We image a thick section (100 μm) of mammary tissue to identify cross sections containing both domains. Images at resonances 2855, 2930, and 3014 cm^{-1} for such a section are shown in Fig. 5(e)–(g), respectively. In this hyperspectral cube of molecular vibrational information, each image pixel contains a spectrum with peak ratios 2930 cm^{-1} /2855 cm^{-1} that fluctuate in between those of collagen and lipids. Because each entire spectrum is collected in a single excitation event (i.e., no tuning is needed for each resonance), the ratio is not subject to variations in the excitation powers or other instability in the system, and it indicates the relative contributions of both domains in

the resulting spectrum. A reconstruction of the molecular composition by domains is shown in Fig. 5(h). This reconstruction simply expresses the spectrum at a given location as a linear combination of two basis spectra, which we take to be those shown in Fig. 5(a) and (b). Finally, an example of this combination is provided. The two basis spectra are added in comparable proportions [see Fig. 5(i)] to reconstruct the spectrum at a purple pixel, shown in Fig. 5(j). The white pixels in the NIVI image [see Fig. 5(h)] had low SNR and did not permit molecular identification.

Although the images in Fig. 5(e)–(g) spatially map the density of CH_2 and CH_3 bonds in the sample, the full consideration of the spectral features provides for a more accurate molecular selectivity. A more rigorous approach could enable NIVI to quantitatively characterize the contribution of different chemical species as clinical diagnostic biomarkers in biological tissues.

Interferometric detection enables signal amplification by increasing the power in the reference arm. The high efficiency of CARS and the use of interferometric detection results in shot-noise-limited signals. With the current acquisition parameters (10 ms integration time, 10 mW pump power, and 2 mW Stokes power), the recovery of spectra is done at a rate three orders of magnitude faster than spontaneous Raman microscopy for a similar SNR of 32 dB. The limiting factor in the acquisition speed in our setup is the speed of the translation stages. To improve this speed, galvanometers can be used. If the camera were operated at 10 kHz, recovery of spectra can be five orders of magnitude faster than spontaneous Raman microscopy, however, the SNR would degrade to 22 dB. Additionally, because this broadband detection scheme is sensitive to the relative spectral phase at the interferometer, it is robust even for thick samples or refractive index variations that may change the path length of the scattered field, provided that dispersion introduced in the setup is compensated.

NIVI is promising for retrieving spectra in the fingerprint region, where peaks are densely populated. In principle, this could enable a wide range of biological and clinical applications requiring high-speed micro-spectroscopy. However, the use of NIVI for *in vivo*, noninvasive or minimally-invasive diagnosis, still faces challenges, such as reducing the complexity of the optical system and developing fiber-based probes for delivery of pulses to the patient. More fundamentally, noninvasive clinical applications require the collection of epidirected anti-Stokes signals, which has been shown to occur only for scatterers smaller than the wavelengths involved, and therefore, retrieval of back-reflected signal from bulk tissue remains to be tested in the future.

We are now investigating methods to expand the spectral window that we probe by the use of supercontinuum generation [22]. In the future, the complexity in the setup could be simplified by using a single pulse configuration [29], [31].

V. CONCLUSION

We have shown the high-speed imaging capability of NIVI for use in biological tissues, and compared the vibrational spectra acquired with NIVI to those from spontaneous Raman

microscopy. By chirping the pump, broadband pump and Stokes pulses are simultaneously used in the acquisition of CARS signals from biological tissue, from which micro-pectroscopic images, instead of intensity images at single resonances, are formed. Rather than seeking to eliminate nontargeted resonances along with the persistent background as in ps-ps schemes or pulse-shaping techniques, we instead acquire the entire vibrational spectrum in a window of 200 cm^{-1} to account for the presence of various resonances and their relative proportions simultaneously, so as to enhance the molecular selectivity. Furthermore, because the resulting signal is linearly proportional to $\chi^{(3)}(\Omega)$, the relative concentration of different chemical species contributing to a spectrum can be discriminated. We provide one example of this differentiation for the case of protein and lipid domains in mammary tissue. In the future, careful identification of the different domains in the fingerprint region could characterize their proportions in tumors or even in premalignant tissues.

ACKNOWLEDGMENT

The authors would like to thank Prof. R. Bhargava and Postdoctoral Fellows M. Walsh, M. Schulmerich, and J. B. Geddes at the Beckman Institute for Advanced Science and Technology, Urbana, Illinois, for their technical contributions to this paper. We also thank F. Nguyen for his assistance with the biological tissue. (<http://biophotonics.illinois.edu/>)

REFERENCES

- [1] J.-X. Cheng, "Coherent anti-Stokes Raman scattering microscopy," *Appl. Spectrosc.*, vol. 61, no. 9, pp. 197–208, 2007.
- [2] M. Delhaye and P. Dhamelincourt, "Raman microprobe and microscope with laser excitation," *J. Raman Spectrosc.*, vol. 3, no. 1, pp. 33–43, 1975.
- [3] Z. Huang, A. McWilliams, H. Lui, D. I. McLean, S. Lam, and H. Zeng, "Near-infrared Raman spectroscopy for optical diagnosis of lung cancer," *Int. J. Cancer*, vol. 107, pp. 1047–1052, 2003.
- [4] M. Gniadecka, H. C. Wulf, N. N. Mortensen, O. F. Nielsen, and D. H. Christensen, "Diagnosis of basal cell carcinoma by Raman spectroscopy," *J. Raman Spectrosc.*, vol. 28, pp. 125–129, 1997.
- [5] A. Nijssen, T. B. Schut, F. Heule, P. Caspers, D. Hayes, M. Neumann, and G. Puppels, "Discriminating basal cell carcinoma from its surrounding tissue by Raman spectroscopy," *J. Invest. Dermatol.*, vol. 119, pp. 64–69, 2002.
- [6] S. K. Teh, W. Zheng, K. Y. Ho, M. Teh, K. G. Yeoh, and Z. Huang, "Diagnosis of gastric cancer using near-infrared Raman spectroscopy and classification and regression tree techniques," *J. Biomed. Opt.*, vol. 13, no. 3, pp. 034013-1–034013-8, 2008.
- [7] N. Uzunbajakava, A. Lenferink, Y. Kraan, B. Willekens, G. Vrensen, J. Greve, and C. Otto, "Nonresonant Raman imaging of protein distribution in single human cells," *Biopolymers*, vol. 72, no. 1, pp. 1–9, 2003.
- [8] N. Uzunbajakava, A. Lenferink, Y. Kraan, E. Volokhina, G. Vrensen, J. Greve, and C. Otto, "Nonresonant confocal Raman imaging of DNA and protein distribution in apoptotic cells," *Biophys. J.*, vol. 84, pp. 3968–3981, 2003.
- [9] M. D. Duncan, J. Reintjes, and T. Manuccia, "Scanning coherent anti-Stokes Raman microscope," *Opt. Lett.*, vol. 7, pp. 350–352, 1982.
- [10] A. Zumbusch, G. R. Holtom, and X. S. Xie, "Three-dimensional vibrational imaging by coherent anti-Stokes Raman scattering," *Phys. Rev. Lett.*, vol. 82, no. 20, pp. 4142–4145, 1999.
- [11] X. S. Xie and E. O. Potma, "Detection of single lipid bilayers with coherent anti-Stokes Raman Scattering (CARS) microscopy," *J. Raman Spectrosc.*, vol. 34, no. 9, pp. 642–650, 2003.
- [12] J.-X. Cheng, Y. K. Jia, G. Zheng, and X. S. Xie, "Laser-scanning coherent anti-Stokes Raman scattering microscopy and applications to cell biology," *Biophys. J.*, vol. 83, pp. 502–509, 2002.
- [13] H. Kano and H. o Hamaguchi, "Vibrationally resonant imaging of a single living cell by supercontinuum-based multiplex coherent anti-Stokes Raman scattering microspectroscopy," *Opt. Exp.*, vol. 13, pp. 1322–1327, 2005.
- [14] X. Nan, E. O. Potma, and X. S. Xie, "Nonperturbative chemical imaging of organelle transport in living cells with coherent anti-Stokes Raman scattering microscopy," *Biophys. J.*, vol. 91, no. 2, pp. 728–735, 2006.
- [15] J.-X. Cheng, H. Wang, T. T. Le, Y. Fu, T. B. Huff, and H.-W. Wang, "Chasing lipids in health and diseases by CARS microscopy," *CACS Commun.*, vol. 1, pp. 13–18, 2007.
- [16] C. L. Evans, X. Xu, S. Kesari, X. S. Xie, S. T. Wong, and G. S. Young, "Chemically-selective imaging of brain structures with CARS microscopy," *Opt. Exp.*, vol. 15, no. 19, pp. 12 076–12 087, 2007.
- [17] T. T. Le, C. W. Rehrer, T. B. Huff, M. B. Nichols, I. G. Camarillo, and J.-X. Cheng, "Nonlinear optical imaging to evaluate the impact of obesity on mammary gland and tumor stroma," *Mol. Imag.*, vol. 6, no. 3, pp. 205–211, 2007.
- [18] J.-X. Cheng, L. D. Book, and X. S. Xie, "Polarization coherent anti-Stokes Raman scattering microscopy," *Opt. Lett.*, vol. 26, no. 17, pp. 1341–1343, 2001.
- [19] C. L. Evans and X. S. Xie, "Coherent anti-Stokes Raman scattering microscopy: Chemical imaging for biology and medicine," *Annu. Rev. Anal. Chem.*, vol. 1, no. 1, pp. 883–909, 2008.
- [20] A. Volkmer, L. D. Book, and X. S. Xie, "Time-resolved coherent anti-Stokes Raman scattering microscopy: Imaging based on Raman free induction decay," *Appl. Phys. Lett.*, vol. 80, no. 9, pp. 1505–1507, 2002.
- [21] G. W. H. Wurpel, J. M. Schins, and M. Müller, "Chemical specificity in three-dimensional imaging with multiplex coherent anti-Stokes Raman scattering microscopy," *Opt. Lett.*, vol. 27, no. 13, pp. 1093–1095, 2002.
- [22] M. Okuno, H. Kano, P. Leproux, V. Couderc, and H. o Hamaguchi, "Ultrabroadband multiplex CARS microspectroscopy and imaging using a subnanosecond supercontinuum light source in the deep near infrared," *Opt. Lett.*, vol. 33, no. 9, pp. 923–925, 2008.
- [23] C. Vinegoni, J. Bredfeldt, D. L. Marks, and S. A. Boppart, "Nonlinear optical contrast enhancement for optical coherence tomography," *Opt. Exp.*, vol. 12, no. 2, pp. 331–341, 2004.
- [24] D. L. Marks, C. Vinegoni, J. S. Bredfeldt, and S. A. Boppart, "Interferometric differentiation between resonant coherent anti-Stokes Raman scattering and nonresonant four-wave-mixing processes," *Appl. Phys. Lett.*, vol. 85, no. 23, pp. 5787–5789, 2004.
- [25] F. Lu, W. Zheng, C. Sheppard, and Z. Huang, "Interferometric polarization coherent anti-Stokes Raman scattering (IP-CARS) microscopy," *Opt. Lett.*, vol. 33, no. 6, pp. 602–604, 2008.
- [26] E. O. Potma, C. L. Evans, and X. S. Xie, "Heterodyne coherent anti-Stokes Raman scattering (CARS) imaging," *Opt. Lett.*, vol. 31, pp. 241–243, 2006.
- [27] Y. J. Lee and M. T. Cicerone, "Single-shot interferometric approach to background free broadband coherent anti-Stokes Raman scattering spectroscopy," *Opt. Exp.*, vol. 17, no. 1, pp. 123–135, 2009.
- [28] S.-H. Lim, A. G. Caster, and S. R. Leone, "Single-pulse phase-control interferometric coherent anti-Stokes Raman scattering spectroscopy," *Phys. Rev. A*, vol. 72, no. 4, pp. 041803-1–041803-4, 2005.
- [29] B. von Vacano, T. Buckup, and M. Motzkus, "Highly sensitive single-beam heterodyne coherent anti-Stokes Raman scattering," *Opt. Lett.*, vol. 31, no. 16, pp. 2495–2497, 2006.
- [30] M. Jurna, J. P. Korterik, C. Otto, J. L. Herek, and H. L. Offerhaus, "Vibrational phase contrast microscopy by use of coherent anti-Stokes Raman scattering," *Phys. Rev. Lett.*, vol. 103, no. 4, pp. 043905-1–043905-4, 2009.
- [31] D. L. Marks and S. A. Boppart, "Nonlinear interferometric vibrational imaging," *Phys. Rev. Lett.*, vol. 92, no. 12, pp. 123905-1–123905-4, 2004.
- [32] G. W. Jones, D. L. Marks, C. Vinegoni, and S. A. Boppart, "High-spectral-resolution coherent anti-Stokes Raman scattering with interferometrically detected broadband chirped pulses," *Opt. Lett.*, vol. 31, no. 10, pp. 1543–1545, 2006.
- [33] C. L. Evans, E. O. Potma, and X. S. Xie, "Coherent anti-Stokes Raman scattering spectral interferometry: Determination of the real and imaginary components of nonlinear susceptibility for vibrational microscopy," *Opt. Lett.*, vol. 29, no. 24, pp. 2923–2925, 2004.
- [34] E. M. Vartiainen, H. A. Rinia, M. Müller, and M. Bonn (2006). Direct extraction of Raman line-shapes from congested CARS spectra. *Opt. Exp.*, [Online]. 14(8) pp. 3622–3630.
- [35] N. Dudovich, D. Oron, and Y. Silberberg, "Single-pulse coherent anti-Stokes Raman spectroscopy in the fingerprint spectral region," *J. Chem. Phys.*, vol. 118, no. 20, pp. 9208–9215, 2003.

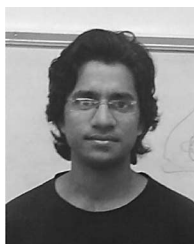
- [36] K. P. Knutsen, J. C. Johnson, A. E. Miller, P. B. Petersen, and R. J. Saykally, "High spectral resolution multiplex CARS spectroscopy using chirped pulses," *Chem. Phys. Lett.*, vol. 387, pp. 436–441, 2004.
- [37] J. X. Cheng, A. Volkmer, L. D. Book, and X. S. Xie, "Multiplex coherent anti-Stokes Raman scattering microspectroscopy and study of lipid vesicles," *J. Phys. Chem. B*, vol. 106, pp. 8493–8498, 2002.
- [38] C. J. Frank, D. C. B. Redd, T. S. Gansler, and R. L. McCreery, "Characterization of human breast biopsy specimens with near-ir Raman," *Anal. Chem.*, vol. 66, pp. 319–326, 1994.
- [39] T. Sakakura, Y. Sakagami, and Y. Nishizuka, "Dual origin of mesenchymal tissues participating in mouse mammary gland embryogenesis," *Develop. Biol.*, vol. 91, no. 1, pp. 202–207, 1982.
- [40] K. B. DeOme, L. J. Faulkin, H. A. Bern, and P. B. Blair, "Development of mammary tumors from hyperplastic alveolar nodules transplanted into gland-free mammary fat pads of female c3h mice," *Cancer Res.*, vol. 19, no. 5, pp. 515–520, 1959.
- [41] V. Gouon-Evans and J. W. Pollard, "Unexpected deposition of brown fat in mammary gland during postnatal development," *Mol. Endocrinol.* [Online]. 16(11), pp. 2618–2627.
- [42] N. J. Kline and P. J. Treado, "Raman chemical imaging of breast tissue," *J. Raman Spectrosc.*, vol. 28, pp. 119–124, 1997.
- [43] H.-W. Wang, T. T. Le, and J.-X. Cheng, "Label-free imaging of arterial cells and extracellular matrix using a multimodal CARS microscope," *Opt. Commun.*, vol. 281, pp. 1813–1822, 2008.



Wladimir A. Benalcazar was born in Quito, Ecuador, in 1983. He received the B.S. degree in physics and electrical engineering from Universidad San Francisco de Quito, Quito. He is currently working toward the Ph.D. degree in the Department of Electrical and Computer Engineering, Beckman Institute, University of Illinois at Urbana-Champaign, Urbana.

Since 2007, he has been with the Biophotonics Imaging Laboratory, Beckman Institute. His current research interest include research in the development

of novel optical techniques for assessing molecular and structural information from cells and tissues.



Praveen D. Chowdary received the B.S. degree in mathematics, physics, and chemistry from Andhra Loyola College, Vijayawada, India, and the M.S. degree in chemical sciences from the Indian Institute of Science, Bangaluru, India. He is currently working toward the Ph.D. degree in the Department of Chemistry, University of Illinois at Urbana-Champaign, Urbana, where he has been engaged in the fields of chemical physics and biomedical imaging.

His research interests include simulation and laser control of molecular vibrational energy flow, as well as the development of nonlinear interferometric vibrational imaging for cancer diagnosis.

Zhi Jiang, photograph and biography not available at the time of publication.



Daniel L. Marks received his graduate degree from the University of Illinois at Urbana-Champaign, Urbana, the M.S. degree in 1995, and the Ph.D. degree in 2001, both in electrical engineering.

He is currently with Prof. S. A. Boppart in the Biophotonics Imaging Laboratory, Beckman Institute for Advanced Science and Technology, University of Illinois at Urbana-Champaign. He has authored or coauthored more than 50 peer-reviewed papers in optics and engineering, and has contributed as a coprincipal investigator on several National Institutes of Health-

funded projects.

Dr. Marks received the National Science Foundation Graduate Fellowship in 1996 for research, the Van Valkenburg Fellowship in 1999. He has received the New Focus Student Award twice in 1999 and 2000.



at Urbana-Champaign.

Eric J. Chaney was born in Mount Vernon, IL, in 1970. He received the B.S. degree in biology from the University of Evansville, Evansville, IN, in 1992.

From 1993 to 1997, he was as a Research Assistant at the Indiana University School of Medicine, Indiana State University, Terre Haute. From 1997 to 2000, he was a Transmission Electron Microscope Technician at the University of Illinois at Urbana-Champaign, Urbana. Since 2000, he has been a Research Specialist in molecular biology at the Biophotonics Imaging Laboratory, Beckman Institute, University of Illinois



Martin Gruebele was born in Stuttgart, in 1964. He received the B.S. and Ph.D. degrees from the University of California, Berkeley.

He was engaged in high-resolution spectroscopy of molecular ions and clusters in the group of R. Saykally. From 1989 to 1992, he was engaged in femtochemistry in the laboratory with A. Zewail in California Institute of Technology, Pasadena and moved to the University of Illinois in 1992. He is currently J. R. Eiszner Professor of chemistry, physics, and biophysics, and computational biology, Beckman Institute, University of Illinois at Urbana-Champaign, Urbana. His research interests include protein and RNA folding, imaging dynamics in live cells, laser spectroscopy of vibrational energy flow in molecules, the theory of quantum computing and quantum control, as well as single-molecule absorption spectroscopy detected by scanning tunneling microscopy.

Dr. Gruebele is a Fellow of the American Physical Society and the Biophysical Society, as well as a recipient of the Coblenz and Wilhelm Bessel Awards, among others. He was elected a Member of the German National Academy of Sciences in 2008.



Stephen A. Boppart (S'90–M'90–SM'06) was born in Harvard, IL, in 1968. He received the B.S. degree in electrical and bioengineering and the M.S. degree in electrical engineering from the University of Illinois at Urbana-Champaign, Urbana, IL, in 1990 and 1991, respectively, the Ph.D. degree in electrical and medical engineering from the Massachusetts Institute of Technology, Cambridge, in 1998, and the M.D. degree from Harvard Medical School, Boston, MA, in 2000.

He was a Research Scientist with the Air Force Laser Laboratory, Brooks Air Force Base, San Antonio, TX, where he was engaged in research on developing national (ANSI) and Air Force laser safety standards. Since 2000, he has been with the University of Illinois at Urbana-Champaign, Urbana, from where he completed residency training in internal medicine in 2005. He is currently a Professor of electrical and computer engineering, bioengineering, and medicine, and the Head of the Biophotonics Imaging Laboratory, Beckman Institute for Advanced Science and Technology, University of Illinois at Urbana-Champaign and also a Leader of a campus-wide Imaging Initiative. He has authored or coauthored more than 165 invited and contributed publications, and more than 400 invited and contributed presentations. He holds more than 25 patents, filed or pending. His research interests include the development of novel optical imaging technologies for biological and medical applications, with particular emphasis on translating these to clinical applications in cancer detection and diagnosis.

Dr. Boppart is a Fellow of the Optical Society of America and International Society for Optical Engineering, the International Society for Optical Engineering, and a Member of the Society for Molecular Imaging, the Academy of Molecular Imaging, the American Association for the Advancement of Science, the American Association for Cancer Research, and the American Medical Association. He was named one of the Top 100 Innovators in the World by the Technology Review Magazine for his research in medical technology in 2002. He received the IEEE Engineering in Medicine and Biology Society Early Career Achievement Award in 2005.